LAWRENCE
LIVERMORE
NATIONAL
LABORATORY

LLNL-TR-817143

Thermo-Mechanical Shock, X-ray Transport and Radiation Response Analysis Experiments on NIF

D. Goto, S. Moon

November 26, 2020

Disclaimer

This work performed under the auspices of the U.S. Department of Energy by Lawrence Livermore National Laboratory under Contract DE-AC52-07NA27344.

ABSTRACT

The study of x-ray induced rapid heating and the resulting material responses - (thermo-mechanical shock (TMS) and thermo-structural response (TSR)) - is important to our understanding of material behavior in extreme environments.

A series of high conversion efficiency (XRCE) x-ray sources have been developed for the NIF laser facility ranging in fluence and spectral content. In conjunction with source development, we have developed a new XTRRA (X-ray Transport and Radiation Response Analysis) test cassette to hold a set of samples, each at equal distance from target chamber center (TCC) where the x-ray source is placed. Design and performance details of the x-ray sources is discussed elsewhere. Here, we describe the development and use of this TMS XTRRA test cassette.

The XTRRA test cassette is a snout mounted on a NIF Diagnostic Instrument Manipulator (DIM) designed to position six samples equidistant from the x-ray source to assure uniform irradiation of all samples. Photon Displacement interferometry (PDI) is used to measure the displacement of the rear surface of each sample resulting from x-ray exposure on the front of the sample. This will help determine the x-ray generated impulse on the sample. The samples are retrieved from the snout after the shot for inspection and post-shot analysis including the measurement of sample ablated mass and engineering tests examining changes in the material structure.

The data from experiments are compared to predictions from LLNL's ASC codes and used to inform models implemented in these codes. Thus, XRCE x-ray sources with the XTRRA snout at the National Ignition Facility (NIF) laser at the Lawrence Livermore National Laboratory [1,2] provide the ability to expose a broad range of material samples directly to high x-ray fluence, measure shock transits, and recover the sample for further analysis post-shot.

INTRODUCTION

Understanding the behavior of materials exposed to high-fluence high-energy x-rays is important for engineering design in extreme environments. Extreme x-ray environments exist in space, in a tokamak, and in the target chamber of NIF. The penetrating x-rays can produce rapid change in the material temperature and strong thermal gradients. Rapid heating of the material or structure can lead to thermo-structural response (TSR) and thermo-mechanical shocks (TMS). The exposed materials can undergo significant damage dependent on a number of factors: the x-ray fluence, the x-ray spectrum, the risetime of the pulse, the duration of the x-ray pulse, the material composition and the structure of that material. For the study of x-ray interaction with materials high x-ray fluence sources across a wide range of x-ray energies are needed [3, 4].

To understand the characteristic response of a given material to a broad range of x-rays we propose focused physics experiments using well-characterized x-ray sources of various intensities and temperatures. This will help us to understand the effects caused by the rapid absorption of x-ray energy and investigate the material response under specific conditions. Then as we measure the response of a material to a well characterized x-ray source, we can test and verify our simulation capability. Subsequently, we can finally generalize the material response to more complex x-ray environments.

X-ray sources meeting these requirements have been developed on the NIF laser. The National Ignition Facility (NIF) is a 192-beam laser system [2] at the Lawrence Livermore National Laboratory capable of delivering up to 1.8 MJ of ultra- violet (351 nm) laser energy to millimeter-scale targets at the center of a 10 m diameter target chamber. A series of high conversion efficiency (XRCE) x-ray sources have been developed for the NIF laser facility. Currently, the available developed sources are Xe-gas, a stainless-steel cavity, Kr-gas, Mo cavity, and Ag nano-wire foam [5].

The development of these high conversion efficiency sources began with the Xe gas pipe [6] with a desire to generate multi-keV x-ray output with energies >3 keV, a pulse width of 5 ns, and x-ray rise-time of order 1 ns. This was achieved using thin-walled (25 μm), 4 mm long, 4 mm inner-diameter epoxy pipes designed to transmit x-rays in the 1-10 keV spectral band. A side-on view of the pipe is shown in figure 1b. Also seen in the figure are the thin (3500 Å) polyimide windows across the laser entrance holes (LEHs). The pipe is filled with 1.2 atm of an Ar:Xe (65:35) mixture and conversion efficiencies for x-ray energy >3 keV is up to 8%. The gas-pipe target described above can be used with a different gas fill changing the output spectrum. Using a Kr gas fill a conversion efficiency of 3% into Kr K-shell (13 keV) radiation can be obtained [8].

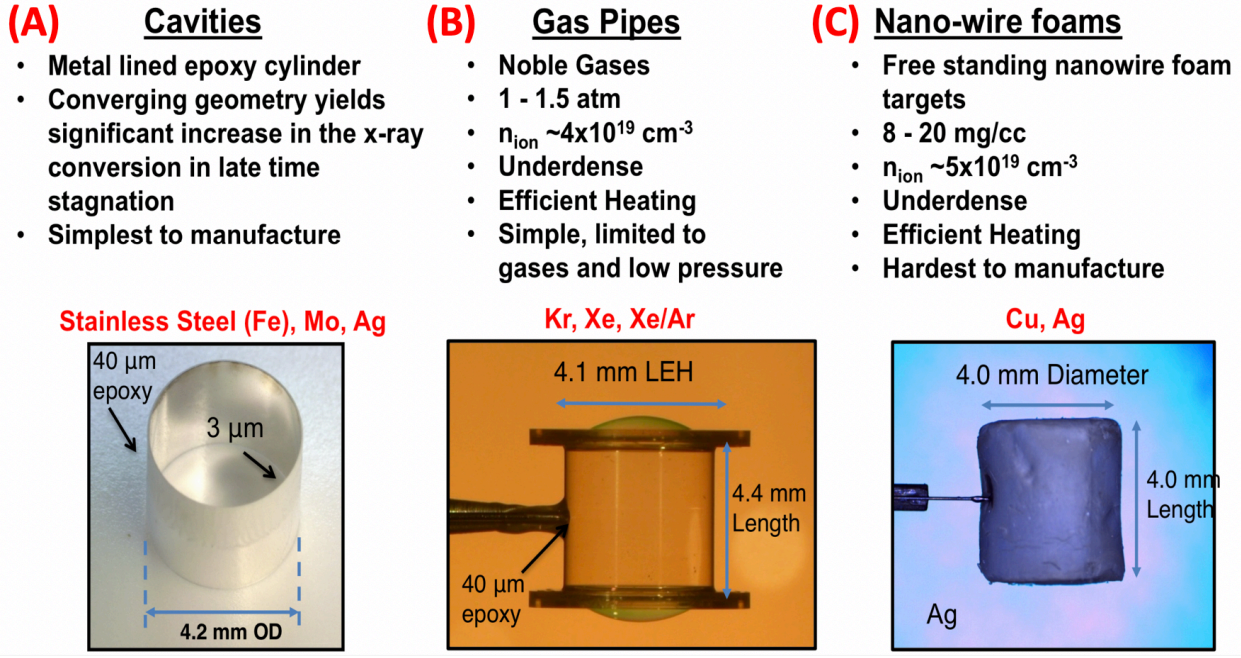

Figure 1. Three types of XRCE source targets are shown: (A) cavities, (B) gas pipes and (C) nano-wire foams. [9]

A metal lined epoxy cylinder was designed in order to obtain higher energy x-ray sources. A bright x-ray stainless steel K-shell source has been developed at the NIF [7] with an x-ray conversion efficiency in the 5-9 keV spectral range of 6.8%. the targets are a 4.1 mm diameter, 4 mm tall hollow epoxy tube having a 50 μm thick wall supporting a thin lining of 3 to 3.5 μm thick stainless steel. The Mo lined target has a measured conversion efficiency of 1%. Nano-wire foams have been made, seen in figure 1c, to achieve a high-Z underdense plasma. The Ag-

foam has a measured efficiency of just under 1% [10]. There is a continued effort to develop higher energy sources and increase the efficiency of the current sources.

In conjunction with efforts to continue to develop higher fluence sources with warmer temperatures, we have developed the XTRRA (X-ray Transport and Radiation Response Analysis) cassette to hold a set of samples, each at equal distance from target chamber center (TCC) where the x-ray source is placed. In section 2 we describe the development and use of the TMS XTRRA snout, the development of the sample holder and the development of the filter layout to both filter the x-ray source and isolate the sample.

Experiments are key to understanding the dynamics of any structure exposed to an extreme x-ray environment. Material analysis in such an environment requires real time (prompt) data and post experiment material analysis. The measurement of material properties such as post-exposure strength, changes in crystal structure, visible damage, cracks, and any deformation of the material are important to our understanding of the behavior of materials in extreme x-ray environments. In section 3 we discuss an experiment using the TMS XTRRA platform to investigate additively manufactured (AM) material in extreme x-ray environments. We discuss the design of the samples, the choice of the sources, and the prompt diagnostics and post shot analysis. In section 4 we conclude and discuss the use of XTRRA with x-ray sources to understand how a material will behave in an extreme x-ray environment.

XTRRA CASSETTE DESIGN

With the development of the XRCE sources NIF provides an ideal experimental facility to test material behavior in an x-ray environment. The NIF gives us the ability to create a high energy x-ray source at TCC and the target chamber becomes an x-ray environment. We need only to place the samples around the source to exposure them to the high energy x-rays. The samples exposed to the high energy x-ray fluence form our material behavior experiments. These experiments use a set of diagnostics to measure the material behavior. The diagnostics such as surface displacement interferometry (PDI) and post-shot recover of the samples for further analysis are discussed in later sections.

The development of the XTRRA (X-ray Transport and Radiation Response Analysis) cassette and sample holder was designed to simultaneously expose a number of independent samples to a similar x-ray environment both in x-ray fluence and spectrum [4,11,12].

To achieve a similar x-ray environment for each of our samples they are placed at an equal distance to the x-ray source. We would like to achieve as large an x-ray fluence as possible which requires to get as close as possible to TCC. We are constrained in how close we can get the samples by their size and limited in reducing the size of the sample by boundary effects from the edges. In addition, the 1 omega unconverted light is of significant intensity and the XTRRA snout must avoid these beams. In the current design we need to support 30 mm diameter samples to limit edge effects and are able to place six samples at a 100 mm distance from TCC.

In figure 2 the XTRRA sample holder is shown in relation to the target positioner. The target positioner positions the XRCE x-ray target at target chamber center (TCC). After the target is positioned the XTRRA snout is positioned into place.

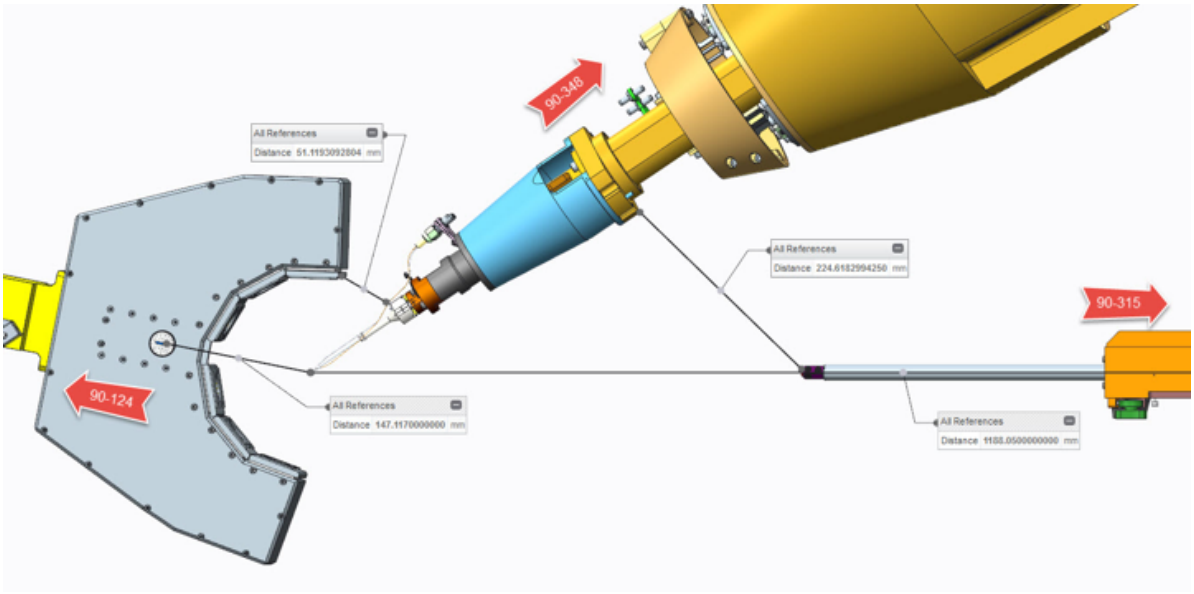

Figure 2: XTRRA sample holder shown in relation to the target positioner and NIF X-ray Spectrometer (NXS) snout. The XRCE x-ray target is positioned at TCC.

The XTRRA and target positioner are shown in figure 3 in relation to the 1ω beams. The design of the XTRRA cassette accounted for the closest safe distance to TCC for a 30mm diameter sample while staying clear of the NIF laser beams 1ω unconverted light. In this design the snout has a nominal clearance of 15.95mm with B115 being the closest beam (12.21mm minimum clearance). This provides a reasonable safety factor ensuring the sample holder received no significant energy from the 1ω light.

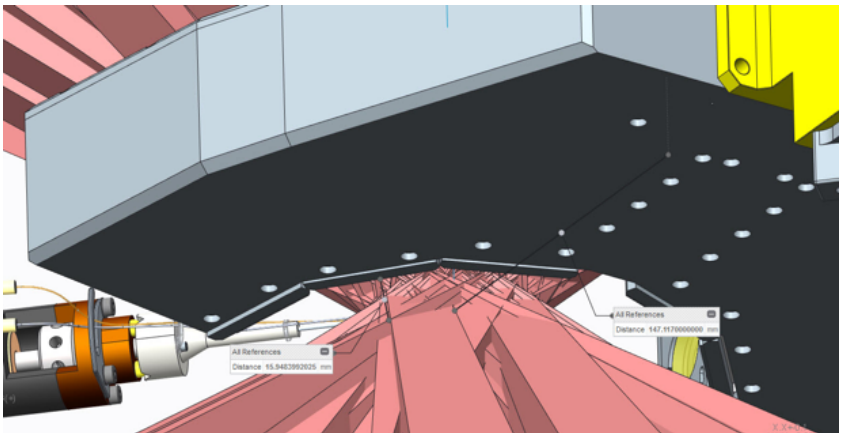

Figure 3: Beam clearances for the 1ω unconverted light

The current XTRRA cassette is capable of fielding 6 samples, each at a closest distance of 10 cm from TCC and each individually diagnosed with a PDI probe. Figure 4 shows the layout of the XTRRA and the locations of the sample holders labeled as “Test Object Holder Assembly.” The alignment brackets are shown labeled “Retro bracket w/ ATLAS Retros.” The quick disconnect mounting block allows for fast replacement of the cassette. The rear of the cassette has the diagnostic cables and PDI fibers.

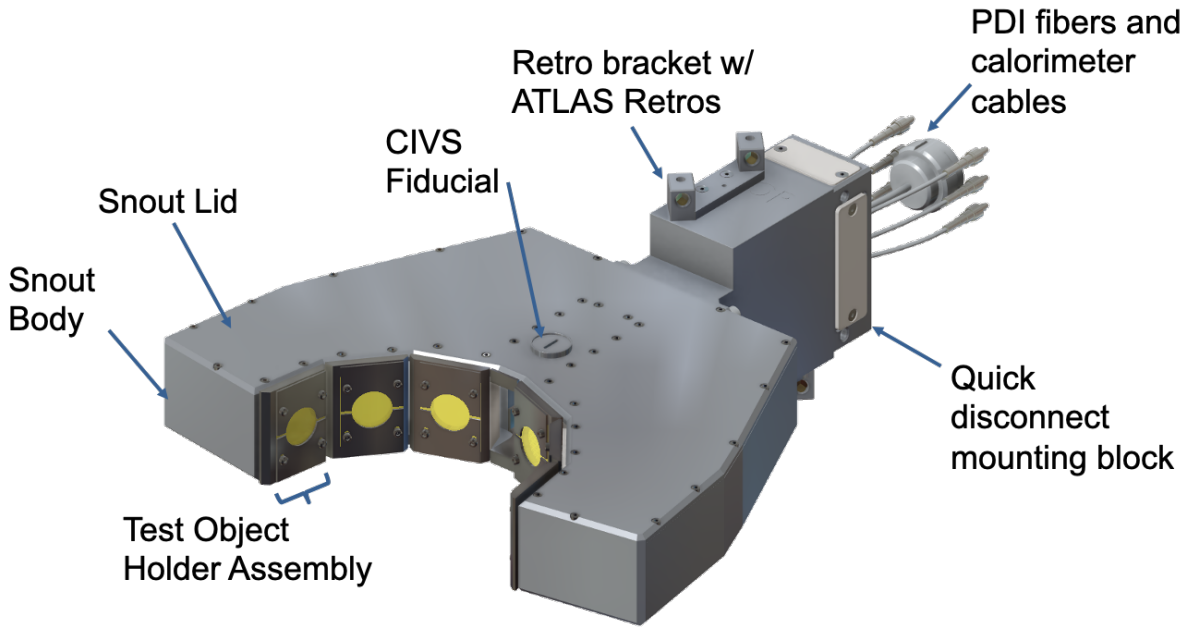

Figure 4: The TMS XTRRA cassette to field the TMS samples

The experimental overview and sample placement are shown in figure 5a. There are 6 different sample assemblies used per snout as seen in the figure. The samples are positioned at line of sight (LOS) 1-6. In this sample holder each LOS are positioned equidistant from the NIF target and pointed toward TCC. Figure 5b shows the XTRRA sample holder the label “sample volume” indicates the location of the sample a volume of 30 mm diameter and 15 mm width, the filter stack is shown, as well as the PDI (Photonic Displacement Interferometry) diagnostic probe. The front surface (TCC-facing) is illuminated by the x-rays, and the resultant displacement and velocity of the back surface of the sample is measured using the PDI probe. In addition, figure 5a CAL 1 shows the placement of a calorimeter. This is used to measure the fluence from the XRCE target at TCC on the target positioner.

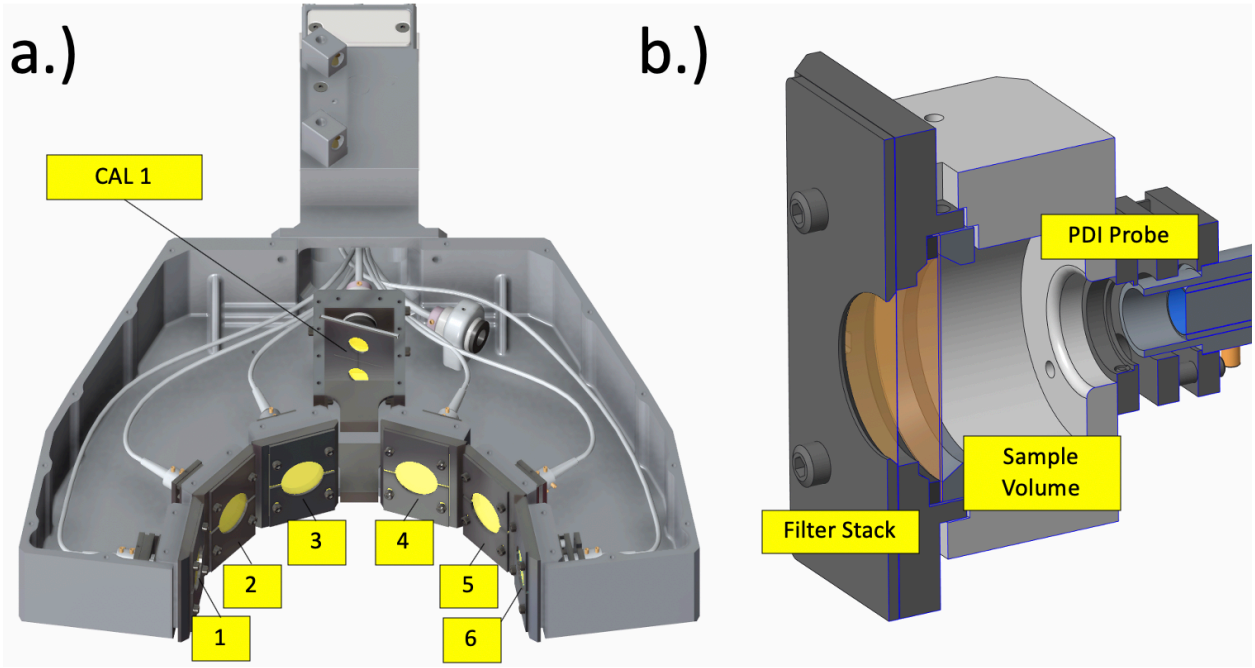

Figure 5: a) TMS XTRRA Snout design with equal sample distances to TCC and b) XTRRA sample holder showing sample volume, PDI diagnostic cable, and a filter stack made up of two filters.

The sample holder is an independent unit and each unit is assembled before placing it into its respective spot in the XTRRA snout. A cross sectional view of the sample holder is shown in figure 5b. The sample can accommodate test samples of 30 mm diameter and 15 mm thick. The sample can be a simple flat disk or a complex 3D structure provided that it can fit into the volume. Larger samples can be fielded with a redesign of the sample holder.

Dependent on the experiment the spectral content of the x-ray source may need to be modified. It is common to remove the low energy x-rays, below 3 to 5 keV, while maintaining the high energy x-rays. To accomplish this, we need to filter the source. In front of the sample, as seen in figure 5b, is a filter stack. This can be a single filter, a series of filters, or no filter at all.

The requirements of the filter are two-fold. The first requirement of the x-ray filter is to modify the spectral content of the source. Since we are interested in the effect of the high energy x-rays it is necessary to remove the low energy spectral component of the source. The second requirement is to isolate the sample from the target chamber and any debris from the XRCE target. An additional requirement is to eliminate or minimize the amount of filter debris, not vaporized, that ends up in the NIF target chamber.

The first requirement to remove the low energy x-rays is a function of the filter material and filter thickness. As an example, for the Kr source, the high energy component that we are interested in preserving is the K-shell emission at 13 keV. The emission spectrum has a large component of energy below 3 keV. Figure 6 shows the reconstructed Dante spectrum. Using a filter made of polyimide 500 microns the red curve in figure 6 shows that the filtered spectrum

below 4 keV is removed and below 10 keV is significantly reduced while maintaining the higher energy 13 keV x-rays.

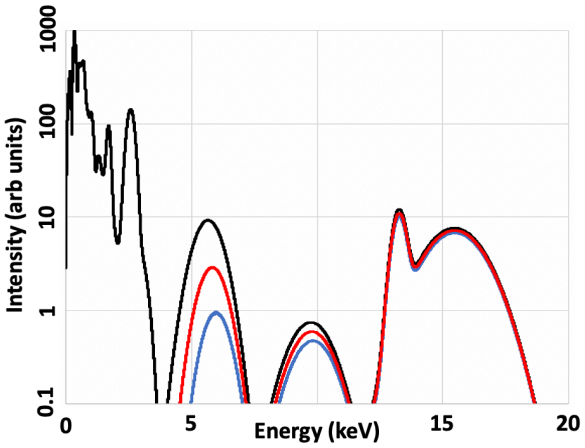

Figure 6: Incident x-ray spectrum Kr target (black), 500 μm of polyimide filtering (red) and 1000 μm (blue).

In addition to filtering the lower energy x-rays the filter needs to remain intact and provide isolation for the sample. The XRCE x-ray source outputs a large amount of energy. At 10 cm from TCC the amount of energy on the filter can be greater than 70 cal/cm^2. The front of the filter will ablate generating a shock and sending remaining filter material toward the sample. If the filter is very thick the strength in the filter material may maintain the integrity of the sample isolation. To make certain that we maintain isolation we have two filters separated by a gap. The first filter is to absorb the majority of the low energy x-rays and the second is to maintain sample isolation. The thickness of the first filter facing the target is designed such that the energy deposited vaporizes the filter. For the case of the Kr-gas target the first filter requires a thickness of less than 100 μm. Using 3 mils (76 microns) of Kapton the front filter will be completely vaporized with a temperature greater than 1500 C. Having the thickness of the second filter greater than 500 μm will ensure the filter integrity and provide an isolated environment for the sample.

EXPERIMENTAL

We have performed a number of experiments using the TMS XTRRA sample holder. Our experimental program has executed four mini-campaigns as of this writing. The first mini campaign consisted of three NIF shots and took place in April 2018 illuminating additively manufactured (AM) materials important to the stockpile stewardship program. The second mini campaign consisting of three shots in February 2019 continued our characterization of the properties of AM materials under rapid x-ray exposure. The third mini campaign of three shots took place in June 2019 and investigated U6Nb material in an x-ray environment. Our fourth mini campaign consisted of four NIF shots. This campaign both continued our investigation of U6Nb and investigated bi-metal samples. In this section, we provide a description of our first mini campaign and the experimental results.

The first mini campaign took place in April 2018 and consisted of three laser shots. The goal was to investigate the structural changes of additively manufactured (AM) Ti lattices due to TMS and TSR generated by rapid x-ray heating. On each laser shot the previously described XTRRA cassette was used providing the same stand-off distance from TCC for each of the six samples on each shot. The three NIF shots used three different x-ray sources from three different targets. The targets used were a Xe-gas filled target, a Kr-gas filled target and a Mo-lined cavity target each generating their respective x-ray source at around 3-5 keV, 13 keV, and 18 keV.

Each source delivered a different x-ray spectrum and also a different fluence. The Xe-gas filled target gives an x-ray source of around 3-5 keV delivering around 70 cal/cm^2 at the sample surface 10 cm from the source with a pulse width of ~2 ns. The Kr-gas filled target delivers an unfiltered source of around 70 cal/cm^2 at 10 cm from TCC with a strong Kr k-shell source at around 13 keV after the low energy x-rays are filtered out. The fluence on the sample surface is around 5 cal/cm^2 with a pulse width of 3.2 ns FWHM. The Mo-lined cavity target delivers an unfiltered source of around 90 cal/cm^2 at 10 cm from TCC with a strong Mo k-shell source at around 18 keV after the low energy x-rays are filtered out with a pulse width of 3.5 ns. The fluence on the sample from this filtered source is around 3 cal/cm^2. Each of these targets can give us a unique understanding of the sample absorption and subsequent behavior to a particular spectrum and fluence. These experiments were the first-time rapid illumination by an x-ray source was employed as a novel approach to characterize additively manufactured parts. This series of experiments included a stress-test of a lattice, measuring the motion of the rear surface and conducting post-shot recovery for additional investigation and testing. The results we have obtained will help improve our understanding of the characteristics impacting the mechanical response to rapid x-ray heating of these unique materials.

The mini-campaign focused on AM Ti lattice material. The sample set for each laser shot was identical consisting of three AM Ti-5553 material samples and three standard Ti-64 material samples. The Ti-5553 AM samples have a material composition of 82.2% Ti, 4.8% Al, 4.8% Mo, 5.2% V, 3% C (wt%) and the standard Ti-64 a composition of 90% Ti, 6% Al, 4% V (wt%). The three standard Ti-64 samples were 0.5 mm flat 30 mm diameter disks. One flat sample was directly exposed to the x-ray source, the second had 250 μm of polyimide bonded to the surface of the Ti-64, and the third had 10 μm of Ni bonded to the surface of the Ti-64. The AM samples consisted of two lattice samples and one AM solid flat. One of the AM lattice sample was manufactured with approximately 9 mm thick lattice structure between two ~0.5 mm solid flat plates (referred to as skins) with a 30 mm diameter. The other AM lattice structure had a single ~0.5 mm solid flat plate with approximately 9 mm lattice structure exposed to the x-rays and 30 mm diameter. The AM solid flat was 0.5 mm thick and 30 mm diameter.

The AM samples were produced using the selective laser melting (SLM) process, a technology that Lawrence Livermore National Laboratory (LLNL) has invested in as part of its growing additive manufacturing efforts. Ti5553 is of specific interest to LLNL since the alloy can possess mechanical properties desirable for programmatic needs while avoiding potential manufacturability concerns such as the formation of a brittle microstructure and high residual stresses during processing (demonstrated for Ti- 6Al-4V). In support of the effort to better understand the mechanical behavior/material properties of SLM-built Ti5553, the goal of this post-shot analysis was to identify deformation as a result of the April 2018 NIF thermo-

mechanical shock experiments as well as any changes in material microstructure that would be indicative of changes to the inherent mechanical properties of the material.

The lattice material investigated can be seen in figure 7. Three different types of Ti5553 samples were used in the experiment: flat disk samples, lattice structures with a single solid flat skin on one side, referred to here as single skins, and lattice structures with solid flat skins on both front and back of the structure, referred to here as double skins. Each type of sample was 30mm in diameter with thicknesses of 0.5 mm, 9.62 mm, and 10.12 mm respectively. Lattice samples were an octet-truss topology with a 10% relative density and 2-unit cells thick. All samples were built on a SLM Solutions 280 series machine and tested in the as-built state (no post-build stress-relief/heat-treat performed prior to the shots).

We investigated a closed structure seen in figure 7b. The structure has a solid flat layer of approximately 0.5 mm thick on both sides of the sample, we refer to these solid flat regions as skins and the sample itself as the double skin sample (figure 7b). The x-rays are deposited on the surface of the skin facing TCC giving rise to a shock or rapid motion that is sent into the lattice structure. To understand the motion that the lattice experienced we also placed a solid flat sample of the same thickness as the lattice skin in one of the sample holders for each of the x-ray sources. Since the fluence was the same for each of the samples on a particular shot this gave us a measure of the dynamic motion subjected to the lattice.

In addition to the double skin lattice, an open lattice structure was investigated, seen in figure 7a. The structure has a solid flat layer or skin of approximately 0.5 mm thick on only one side of the AM lattice. The sample was placed in the sample holder such that the open lattice faced toward TCC and was exposed to the x-ray source. The x-rays deposit their energy on the lattice structure and also on the rear of the lattice skin where the surface had a line of site to the x-ray source.

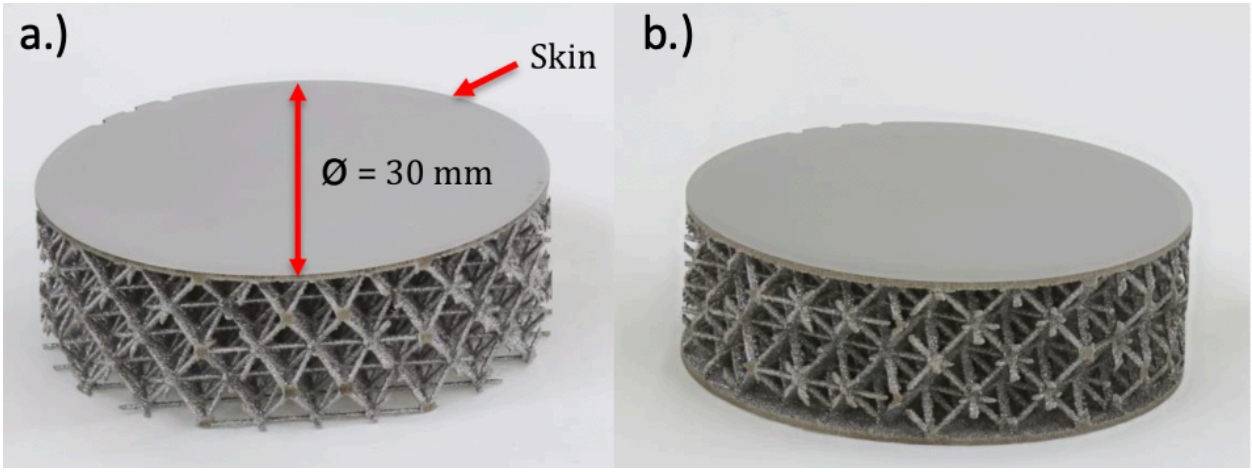

Figure 7: Example of single skin (a) and double skin (b) lattice samples before the shots. The skin on the samples is 0.5 mm thick and the lattice structure is 10 mm thick and has a 30 mm diameter.

These samples were characterized before and after the shots using computed tomography, optical microscopy/metallography, scanning electron microscopy, and energy dispersive x- ray spectroscopy, deformation of the samples and changes to the material microstructure were identified. Prior to the shots, the geometry of the lattice samples was inspected using optical microscopy and computed tomography (CT). After the shots, macroscale deformation of the samples was assessed using optical microscopy and CT. Metallographic mounts were also prepared and optical microscopy, microhardness testing, scanning electron microscopy (SEM), and energy dispersive x-ray spectroscopy (EDS) were performed to determine whether significant changes to the material microstructure, which can be indicative of changes to the mechanical properties of the material, occurred as a result of the shots.

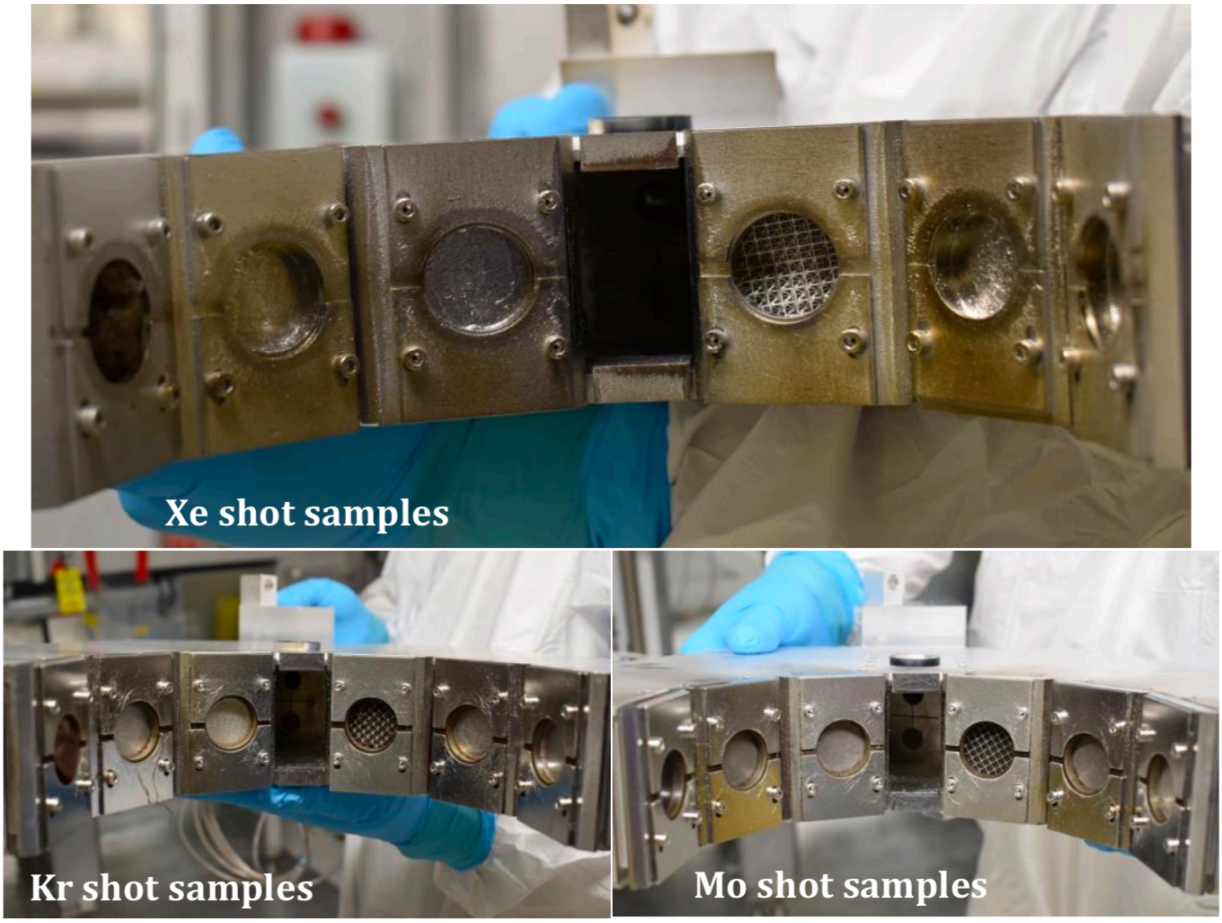

Figure 8: Images of samples within the assembly taken after each shot.

Post-shot images of the samples are provided in Figure 9. Due to the fixturing of the samples, the directly irradiated region was approximately 25 mm in diameter and is identified by a discolored/rough surface. The color of the irradiated surface varied according to the target source and was consistent among sample types. Blowback of the Kapton filter into the irradiated surface was observed for the samples from shots #2-3 with the Kr and Mo source.

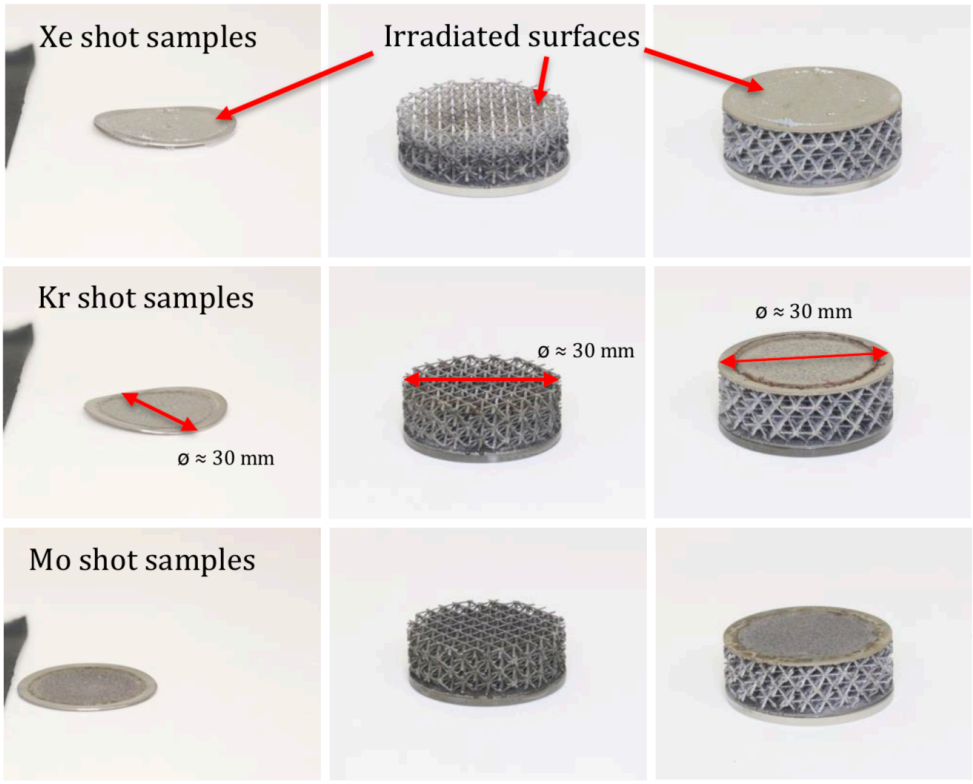

Figure 9: Post-shot images of Ti5553 samples from the Xe (top row), Kr (middle row), and Mo (bottom row) shots. Deformation is particularly visible for the Ti5553 skins.

All Ti5553 AM flat samples exhibited deformation as a result of the shots. All of the single skin lattice structures were damaged as a result of each shot evidenced by numerous broken or deformed struts throughout the structures near the sample boundaries. Lattice material for the double skin structures appeared unaffected by the Xe/Kr shots, while the sample from the Mo shot (18 keV peak x-ray energy) experienced deformation of the struts near the sample boundaries

In addition to sample characterization, we were able to measure the displacement of the sample during the experiment. This prompt data was obtained using a Photon Displacement Interferometer (PDI). This diagnostic takes a measurement of the rear surface displacement and gives us a measure of the impulse generated from the x-ray absorption. Figure 10 shows displacement and velocity of the standard Ti-64 flat samples from three NIF shots using Xe, Kr, and Mo targets. The flat samples were 0.45 mm thick Ti-64 of standard manufacture. These samples are similar to the Ti-5553 AM samples shown in the left column of figure 9. All the samples were backed by PMMA. The PMMA is placed on the back to reduce the possibility of spall. The PDI measurement is taken from the interface between the Ti/PMMA interface. The Xe x-ray source is not filtered and has a fluence of over 70 cal/cm^2. Considering the attenuation cross section for Ti at 4-5 keV is 1e4 cm^2/g the effective depth of the energy deposition is ~0.2 microns. This would give an average energy per gram of 1e5 J/g exceeding the heat of vaporization of 8,800 J/g. This ablates the front of the Ti sample generating a shock that imparts

an impulse into the sample. Figure 10 shows the measured PDI displacement and velocity in comparison to the simulation for the standard Ti-64 flat. Figure 10a shows the displacement of the reference Ti-64 sample for the Xe target source. The magnitude of the initial displacement of the back surface of the Ti flat sample of 7.38 μm from the PDI measurement allows us to calculate an impulse of 1.13 ktap. The unit tap is a measurement of momentum change in cgs units (1 tap = 1 dyne-sec).

In figure 10b the displacement and velocity taken from the standard Ti/PMMA interface for the Kr x-ray source. The Kr-gas source is filtered with a 250 μm Kapton filter to remove the low energy, below 4 keV, x-rays. The filtered Kr source main consists of the K-shell emission of 13.2 keV x-rays with a fluence of 4 cal/cm^2. The attenuation cross section for Ti at 13.2 keV is 70 cm^2/g the effective depth of the energy deposition is 32 microns. This would give an average energy per gram of 720 J/g well below the heat of vaporization of 8,800 J/g but above the heat of fusion of 400 J/g. The fluence is not high enough to ablate material from the Ti but it can melt the surface and generate a structural response. The thermal structural response (TSR) can be seen in the data as the rapid motion of the back surface.

The Mo x-ray source PDI data is shown in the bottom row of figure 10. These two plots show the displacement and velocity for the Ti flat/PMMA interface. This source is filtered by a 250 μm Kapton filter to remove the low energy, below 4 keV, x-rays. The filtered Mo source consists mainly of the Mo K-shell 18 keV photons with a fluence of 4 cal/cm^2. As with the Kr source, the Mo source does not have sufficient energy to ablate the Ti. It does have enough energy to rapidly heat the Ti and generate TSR. This can be seen in the data as the rapid motion of the back surface.

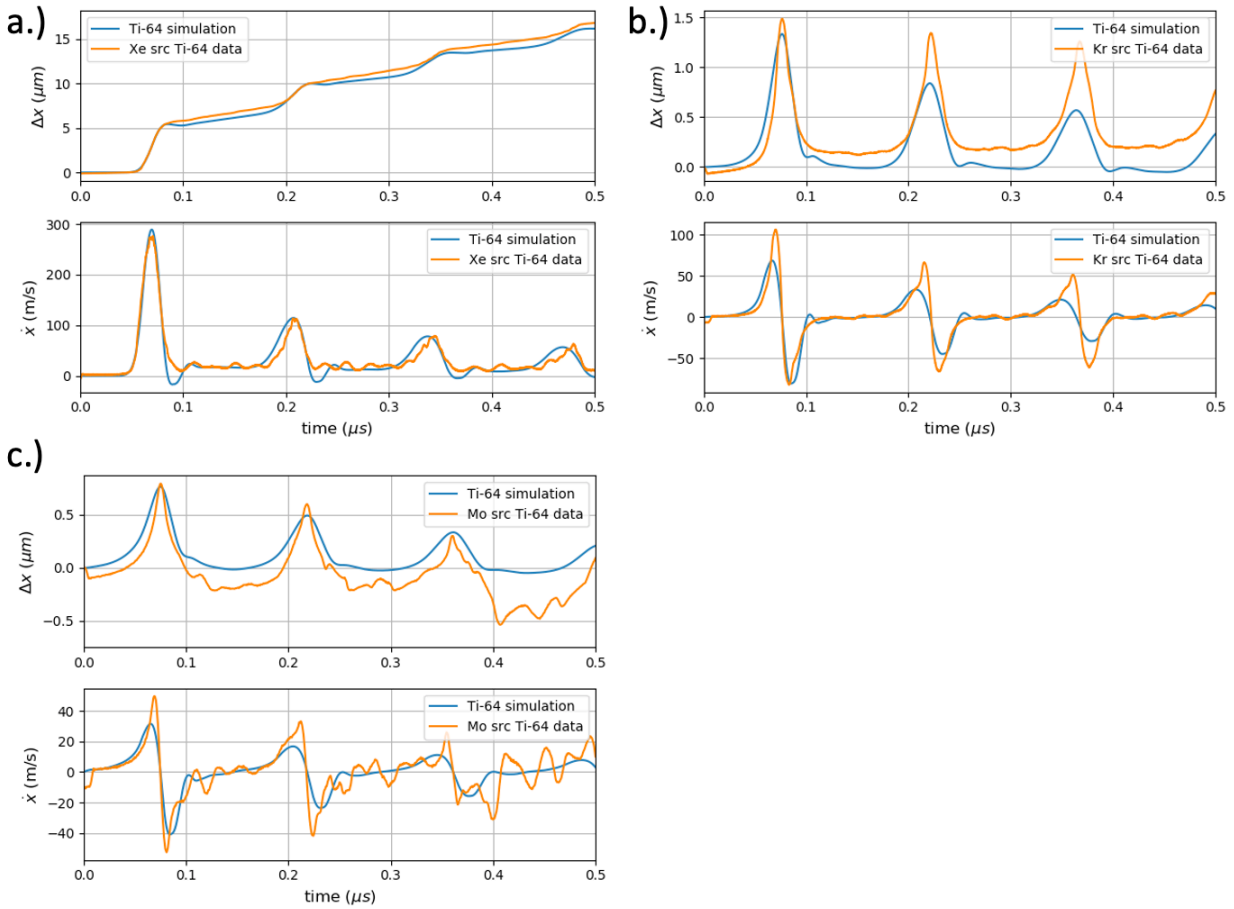

Figure 10: Ti sample rear surface displacement and velocity as measured by PDI. There is a dependency on EOS and strength parameters. Leos for Ti-64 and a SG strength model with pmin -0.036 and etamin 0.87 to match data. The Xe-source is the measured source 72.6 cal/cm^2, the Kr is using the measured source at 69.8 cal/cm^2, and the Mo at the measured fluence is 91.4 cal/cm^2. These are for (a.) N180424-001, (b.) N180424-002, and (c.) N180425-001 respectivly.

Inspection of the samples using a Zeiss SteREO Discovery.V12 stereomicroscope was performed to observe strut deformation resulting from the shots. Visible deformation of diagonal struts in the unit cells closest to the irradiated surface was evident for each of the single skin lattices (Figure 11). Deformation of the double skin lattices appeared minimal and was investigated further with CT.

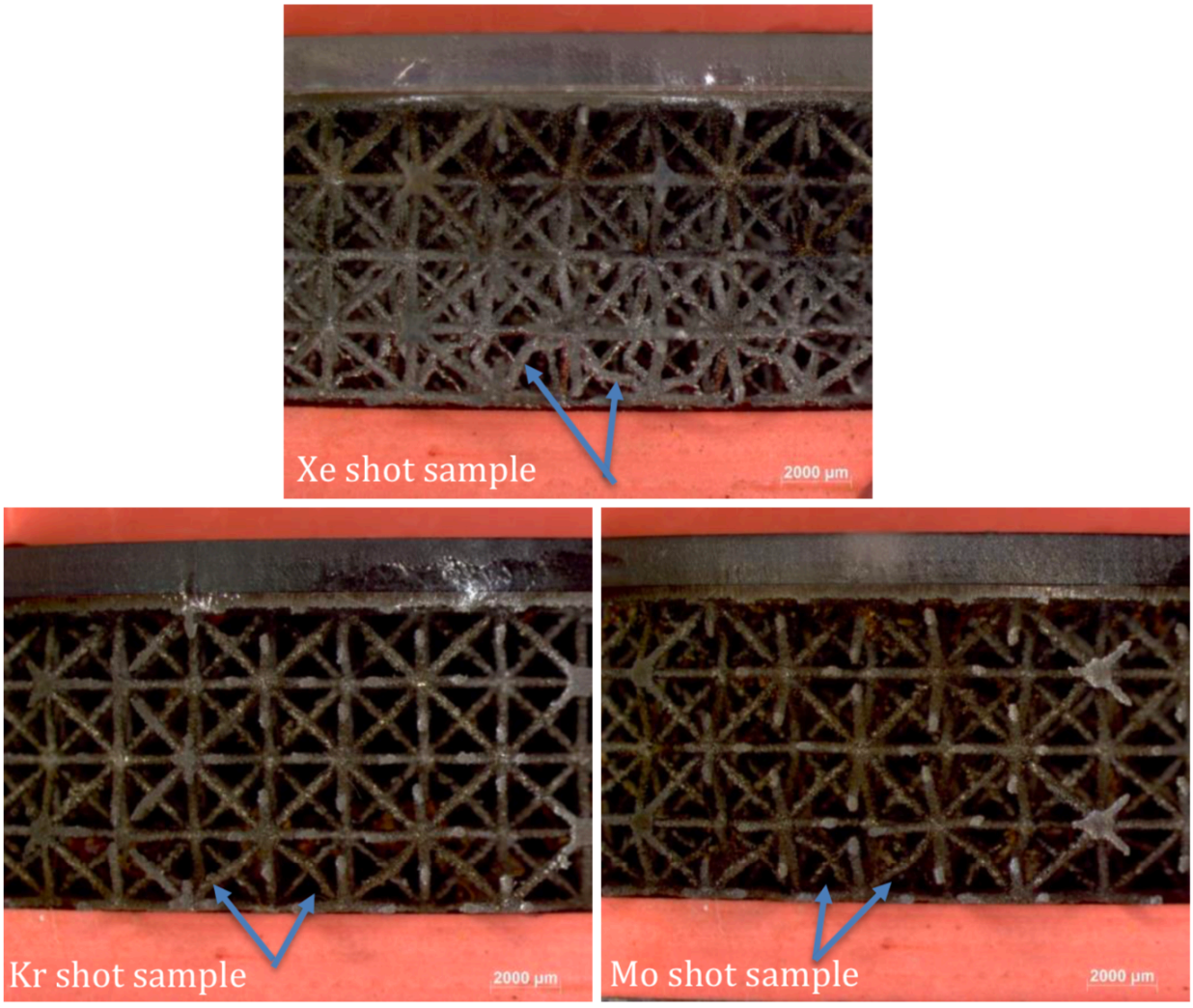

Figure 11: Post-shot images of the single skin lattices from each shot. Each sample exhibited significant plastic deformation of the struts near the irradiated surface (indicated by arrows).

The post-shot sample characterization began with visualizing the parts. To visualize broken struts and deformation throughout the entirety of the lattice structures, CT (Computed Tomography) data was collected using a NSI X25 machine. Cross-sectional images produced from the CT data were inspected and isosurfaces of each sample were created in AvizoTM Lite software. To create the isosurfaces, a stack of sample cross- sectional images (8bit grayscale) were imported into the software and a threshold was specified for the images. The voxel size used to specify geometric resolution was 23.1 µm.

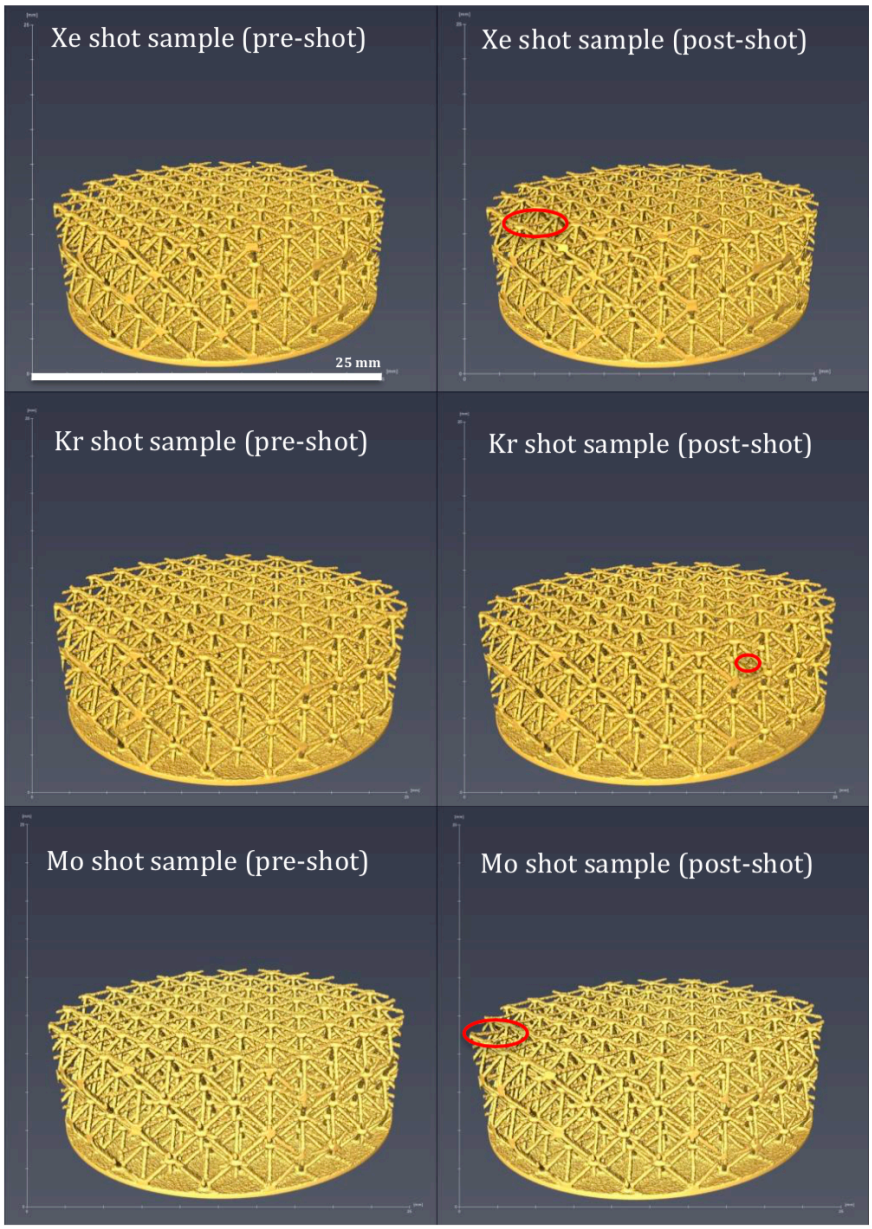

Figure 12: Isosurfaces created using CT data taken of the single skin lattices before/after the shots. Yellow is an artificial color to represent the surfaces of the samples. Each sample exhibited significant deformation of the struts near the irradiated surface. Examples of broken struts are shown in red. Scalebar determined using near surface of sample as focal point.

Deformed and broken struts were visible for the single skin lattice samples from each shot (Figures 12 and 13). However, strut deformation and breakage were restricted to the unit cell of struts closest to the irradiated face. Strut deformation and breakage was concentrated beneath the region constrained by the sample holder (outside of the directly irradiated area, near the sample boundaries). Significant bowing of the horizontal struts at the irradiated surface was observed for

the Kr and Mo shots, but the extent to which this result is influenced by blowback of the Kapton filter into the samples is unknown.

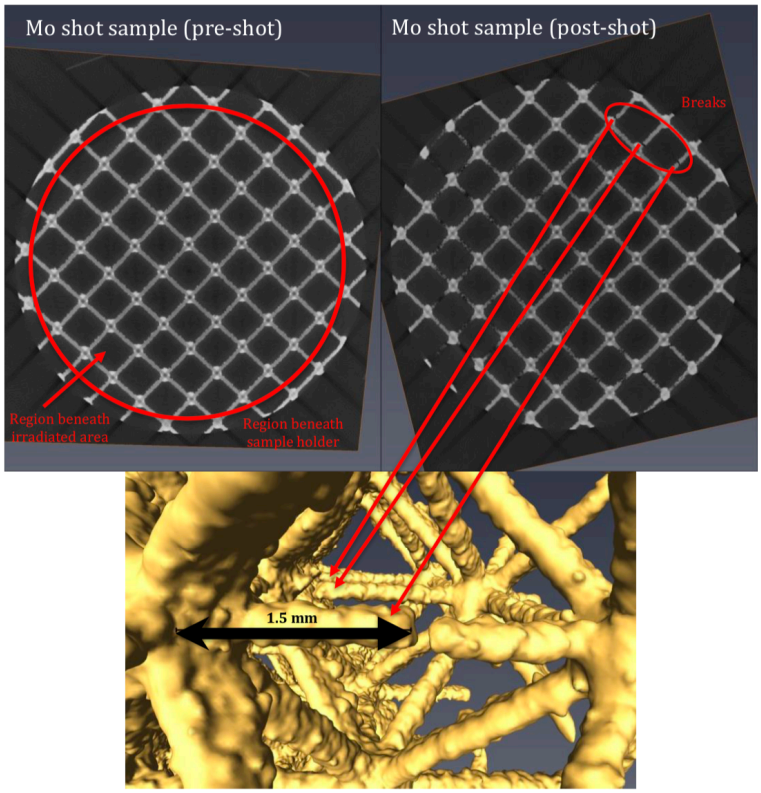

Figure 13: Example of using CT images to locate broken struts within a lattice structure. Cross-sectional slices corresponding to the second row of horizontal struts below the irradiated surface of the single skin lattice from the Mo shot are shown (above) with the associated isosurface (below). Broken struts are identified in red as well as a superimposed approximation of the irradiated area. The surface rendering also shows the high degree of surface roughness on the struts from the AM process. It should be noted that the dark regions inside the nodes are artifacts of the tomographic imaging process and do not represent porosity. Scalebar determined using closest broken strut as focal point.

For the double skin lattice samples, strut deformation and breakage was only observed for the sample from the Mo shot (Figure 14). Deformation and breakage was again restricted to the outer region of the sample constrained by the sample holder, with no appreciable deformation of the internal struts beneath the irradiated area. However, strut deformation was visible throughout the entire thickness of the lattice section for this sample.

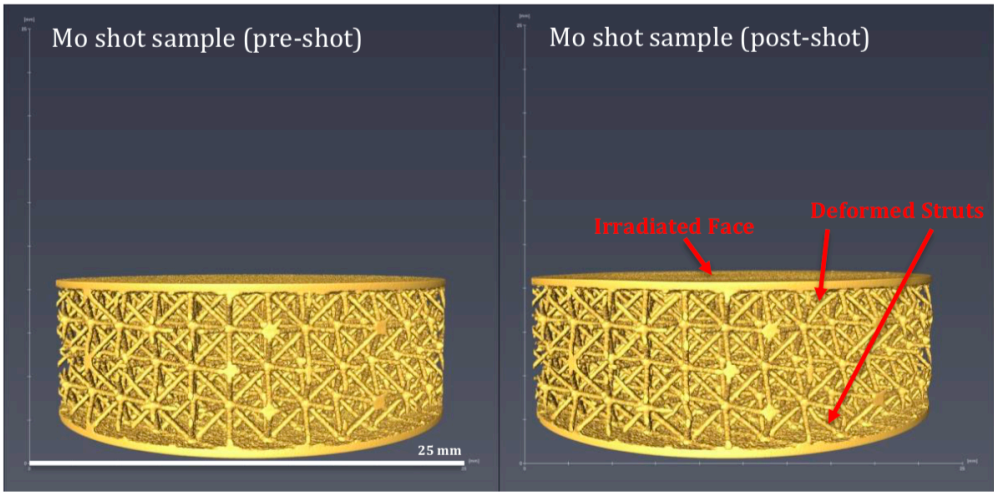

Figure 14: Isosurfaces created using CT data taken of the double skin lattice before/after the Mo shot. Strut deformation is observed throughout the full thickness of the lattice. Scalebar determined using near surface of sample as focal point.

Metallography was performed on polished and etched cross-sections of the Ti5553 skins, single skin lattices, and double skin lattices to determine whether there were any changes in the material microstructure due to the shots. Microstructural differences such as changes in grain size, grain morphology, and the presence of new crystalline phases can result in changes to the mechanical properties of the material.

For reference, untested Ti5553 material was also prepared and examined using a Keyence VHX-5000 microscope (Figure 15). Since the size and shape of the grains for AM parts can vary significantly depending on whether the material is sectioned perpendicular to, or along the build direction, two pieces were prepared in such orientations from the bulk reference material. Elongation of the grains along the build direction is observed for the bulk reference material, which is often reported for AM metals in literature [13-14]. Grains in the cross-section perpendicular to the build direction are more equiaxed in nature. The measured grain size for the bulk reference material varies significantly depending on the observed orientation; grains observed perpendicular to the build direction are typically <100 μm in size while grains observed along the build direction are often hundreds of microns in size. Reference lattice material was prepared as well (Figure 16) and displayed
grain morphology similar to the bulk sample oriented perpendicular to build direction. The optical micrographs suggest a fully β-phase microstructure for all reference material which agrees with what has been reported for as-built AM Ti5553 [14].

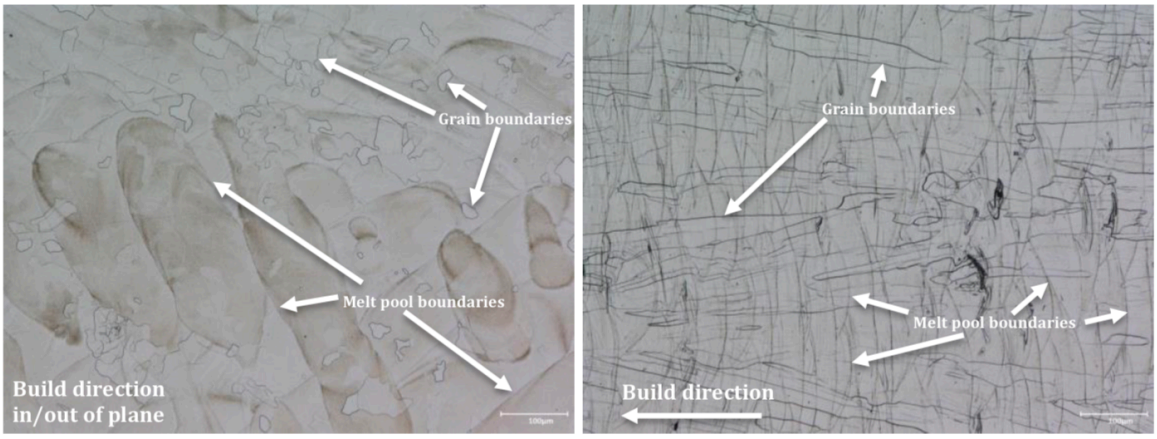

Figure 15: Micrographs of Ti5553 bulk material sectioned perpendicular to (left) and along (right) the build direction. Grains appear elongated along the build direction and more equiaxed when observed perpendicular to the build direction. Melt pool boundaries from the selective laser melting process are also visible.

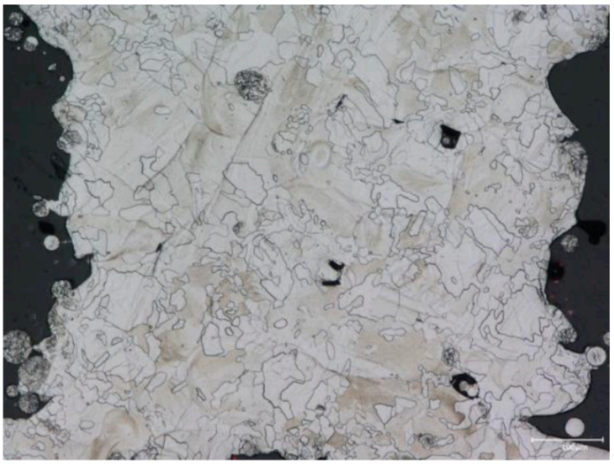

Figure 16: Micrograph of a node of reference Ti5553 lattice material. Satellite particles can be observed near the edges of the material.

Micrographs of the Ti5553 skins are shown in Figure 17. Each sample possesses a visible surface layer at the irradiated face. Depending on the shot, the morphology of the surface layer may be influenced by foreign material impacting the sample surface at high speed (Kr and Mo shots), or re-solidification of material due to high temperatures generated at the irradiated surface (melting of the irradiated Ti5553 sample surface was expected for the Xe shot). The surface layers are uneven in thickness across the surface, but the maximum depth of the surface layer among the samples appears to be ≈50 μm. The surface layer appears thinnest for the Mo shot sample consistent with the lower x-ray fluence. The grain morphology of the bulk material beyond the surface layer appears largely unaffected by the shots, however, regions with acicular features (Figure 18) were present for the Xe and Mo shot samples. These features may be indicative of the plastic deformation response of the as-built material since similar features were observed near a sheared surface of one of the reference pieces (Figure 19).

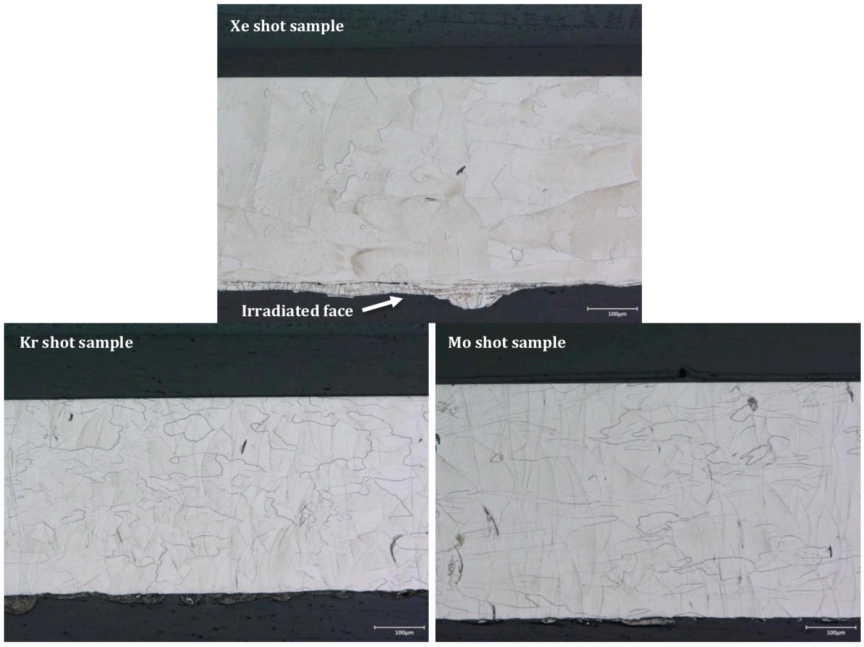

Figure 17: Micrographs of cross-sections of the Ti5553 skins from each shot. A surface layer is visible at the irradiated face for all samples.

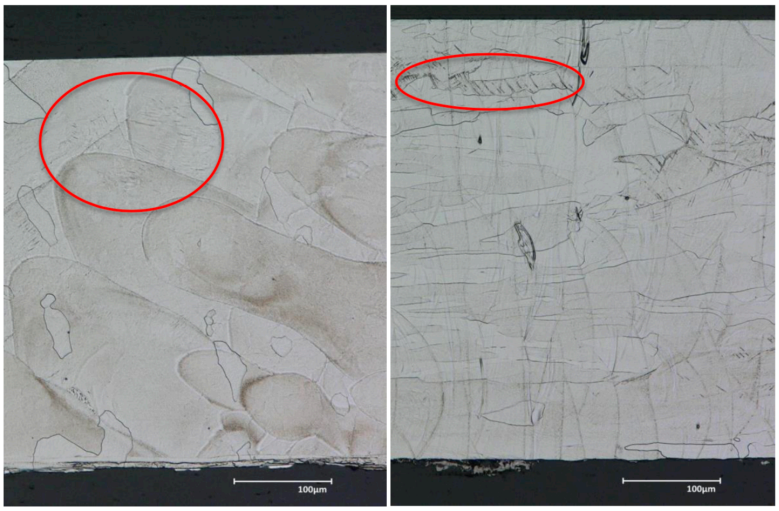

Figure 18: Micrographs of Ti5553 skins from the Xe (left) and Mo (right) shots. Examples of the acicular features within the microstructure are circled.

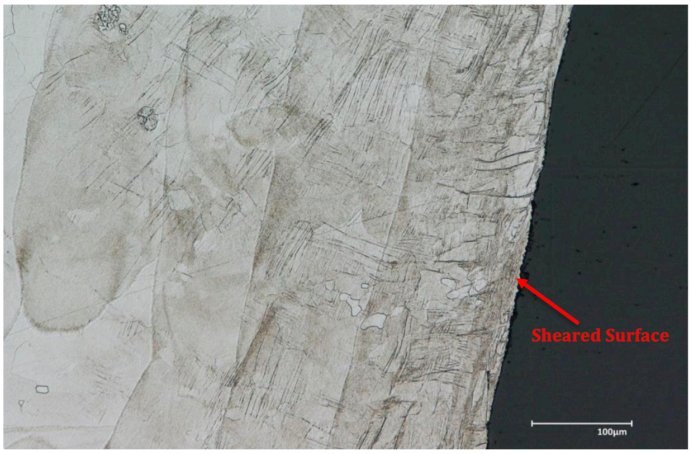

Figure 19: Micrograph of one of the Ti5553 reference pieces showing a surface that was sheared as part of sample preparation. Acicular features present near the sheared surface may be indicative of stress-induced α" which is reported in literature as a deformation mechanism of the alloy [6].

The single and double skin lattice samples examined also possessed surface layers similar in appearance to those of the Ti5553 skins. The grain morphology of the bulk lattice material away from the surface layers also appeared largely unaffected by the shots. Unlike the single skin lattice samples, surface layers for the double skin lattice samples did not extend into the lattice material. To further characterize the surface layers, SEM/EDS was performed on the Ti5553 skins from Figure 18.

All samples from each shot exhibited changes in the surface at the irradiated side of each sample. This manifest itself as a visible surface layer, seen in figure 17, of variable thickness (max thickness ≈50 μm). There were no large changes in average hardness (>10 HV) were measured between the reference Ti5553 material and the Ti5553 skins after each shot. In addition to the β grains seen in the bulk material beyond the surface layers, acicular features were visible within the bulk material for the samples from the Xe and Mo shots. Since acicular features were also observed in deformed reference material, it's possible these features are indicative of the plastic deformation response of the material. No phases other than β and potentially stress-induced α" are apparent in the microstructure of the samples inspected post-shot and β grain size/morphology appeared unchanged. As a result, no significant changes to the yield strength of the bulk material are expected as a result of the x-ray illumination.

It was found that regions of high iron and nickel content were present in the surface layers for samples from each shot not seen in the preshot characterization. This suggests contamination of the surface occurred during the shots (the stainless steel sample holder is a possible source of contamination). Contamination of the sample surface also occurred for the Kr/Mo shot samples due to blowback of the Kapton filter into the sample surface. It should be noted that shots #2-3 utilized a Kapton X-ray filter (≈0.25 mm thick) in front of the samples. The first shot, Xe source, did not have a filter and it was exposed to the target debris. Each sample was also positioned at equal distance from the target chamber center (TCC) as shown in figure 2 such that for a given shot, each sample experienced equal x-ray fluence.

Vickers microhardness measurements were taken using a LECO LM300AT microhardness tester across the surfaces of the Ti5553 skins (8 indents per sample) and reference material (5 indents) since differences in hardness can be indicative of microstructural changes that cannot be observed with the optical microscope. For instance, some phases observed in Ti-alloys such as ω or α may be present within a microstructure, but not resolvable at low magnification. If present in significant quantities, these phases can lead to increases in yield strength, embrittlement of the material, and large increases in average hardness (≈30-220 HV) relative to a primarily β microstructure [15-16]. Since the stress vs. strain data for as-built Ti5553 suggests no large increase in average hardness would be expected to result from the shots from simple plastic deformation alone (given lack of strain hardening post-yield), hardness measurements can provide qualitative information on whether significant changes to the material microstructure or yield strength are likely due to the shots.

Microhardness results for the Ti5553 skins are presented in Table 1. Regions near the surface layer and further into the bulk were indented. The surface layers themselves were not indented since accurate interpretation of a hardness measurement would require the layers to be continuous throughout the interaction volume with the indenter, which cannot be assumed. As a result, the mounting epoxy would likely influence hardness measurements for the surface layers.

Table 1: Microhardness measurements for the Ti5553 skins and reference material (performed using a 50g load).

Sample ID	Avg. hardness (HV)	Std. deviation (HV)
Reference Piece	304	9
Xe shot skin	313	8
Kr shot skin	304	10
Mo shot skin	307	9

No large differences in average microhardness were observed between the bulk reference material and the bulk material for each Ti5553 skin (all means within 10 HV). However, since there were some regions within the bulk containing acicular features (Figure 18), regions containing these features were indented for the Xe and Mo shot samples as well as the reference sample with known deformation (Figure 19). While indenting the acicular regions did not yield large differences in hardness compared to the average values recorded for each sample (<30 HV difference), it's possible that the acicular features may correspond to stress-induced α" which is reported as a deformation mechanism for Ti5553 with an initial primarily β microstructure [18]. Verification of this hypothesis would require further investigation using additional characterization techniques such as x-ray diffraction or transmission electron microscopy. Overall, the hardness measurements did not provide evidence for the widespread formation or growth of additional crystalline phases such as α, ω, or α' within the Ti5553 skins that are associated with large increases in strength and loss of ductility relative to an initial β microstructure [17, 19]. The presence of α and α' are particularly unlikely for these samples since α typically forms via nucleation and growth (too slow given the timescale of the shots) and

martensitic α’ formation upon rapid cooling is reported to be suppressed for beta alloys such as Ti5553 [20].

Since samples from each shot exhibited a distinct layer at the irradiated surface, the metallographic mounts for the Ti5553 skins were examined further using SEM/EDS to better understand the nature of this layer.

SEM allows for higher resolution imaging of the samples by placing a sample under an electron beam and detecting the electrons emitted from the sample. Backscattered electron (BSE) images were taken since they can provide image contrast based on compositional differences in the sample (atomic number influences the number of BSEs reaching the detector). Since the samples analyzed were polished flat, topographic contribution to signal intensity is minimal. As a result, bright areas in an image correspond to regions enriched in elements of higher atomic number while darker regions may correspond to regions containing elements of lower atomic number or porosity.
EDS provides chemical composition information by analyzing characteristic x-rays emitted by the sample due to interaction with an electron beam. Upon collecting x- ray data, a spectrum corresponding to the counts of collected x-rays vs. their energies is created and weight percentages of each element within the analyzed region can be calculated. Composition calculations performed by the software are influenced by many factors such as sample density, homogeneity, surface roughness, and which elements are identified as present within the spectra. Due to a lack of available calibration standards for the instrument and uncertainty in the surface layers being fully dense/homogenous throughout the e-beam interaction volume, all EDS comparisons that will be presented should be considered qualitative in nature.

A SEM image and EDS measurement of the reference sample taken with a Phenom ProX microscope are shown in Figure 20. All of the primary alloying elements of Ti5553 (Al, Mo, V, Cr, and Fe) can be identified within the EDS spectrum. No appreciable Ni was found, but the expected locations of the Ni peaks are shown for future reference. Overall, the measured spectrum is considered a fair representation of the bulk material.

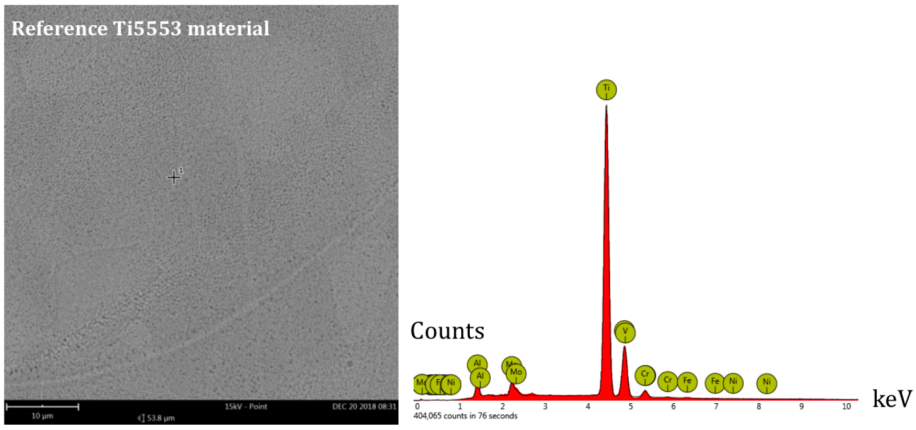

Figure 20: SEM image (left) and EDS spectrum (right) taken from bulk Ti5553 reference material. Crosshair corresponds to the location of the EDS measurement.

A SEM image as well as EDS measurements of the Ti5553 skin from the Xe shot are shown in Figure 21. The EDS measurement taken far away from the irradiated surface (25pprox.. 40 µm) agrees with the spectrum from the reference Ti5553 sample. However, the layer near the irradiated surface appears very bright, suggesting this region contains a significant concentration of elements with higher atomic numbers than surrounding regions. Strong peaks corresponding to iron and nickel are present in the EDS spectrum taken from the surface layer, validating this claim. Since the composition of Ti5553 contains <1 wt% iron and negligible nickel, the strong Fe/Ni peaks in the EDS spectrum are likely caused by surface contamination. Upon inspecting Figure 10 further, ablation of the 304 stainless steel sample holder likely occurred as a result of the shots, causing large amounts of iron and nickel to interact with the surface of the sample.

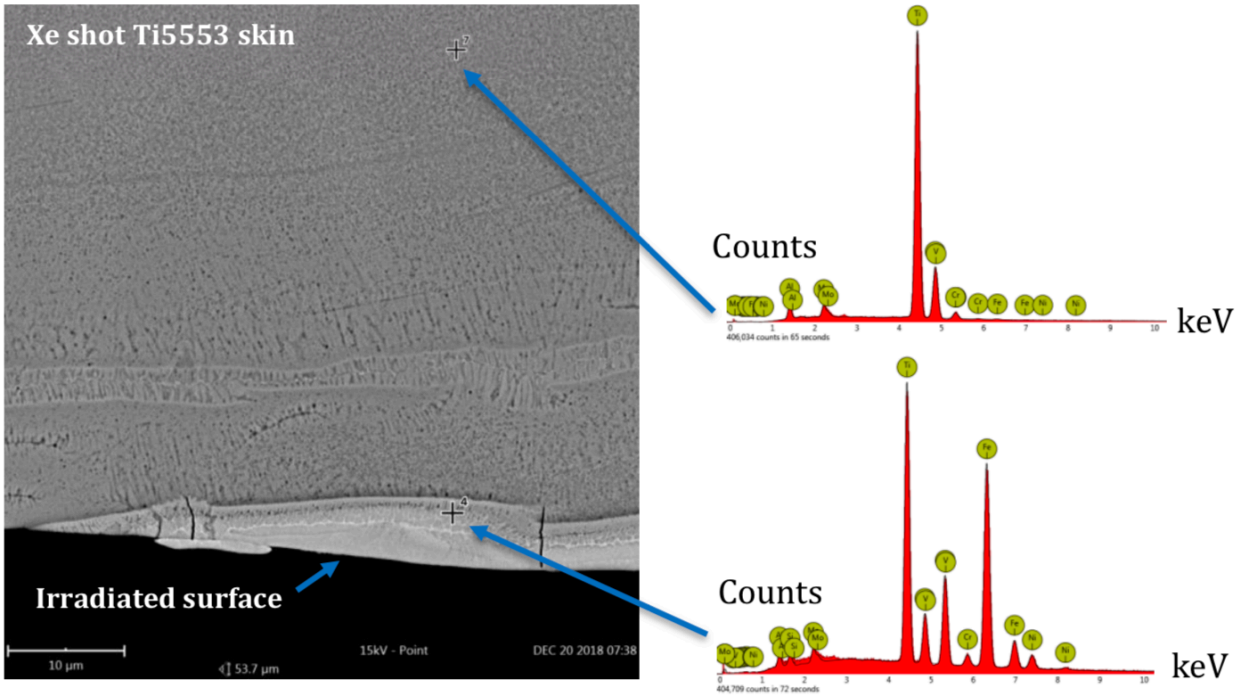

Figure 21: SEM image (left) and EDS spectra (right) of the Ti5553 skin sample from Xe shot. Crosshairs correspond to locations of EDS measurements. The surface layer spectrum shows strong Fe/Ni signals.

SEM images of the Ti5553 skins from the Kr and Mo shots exhibited two surface layers (Figure 22). EDS measurements taken of the surface layers with dark contrast yielded EDS spectra similar to the reference Ti5553 spectrum. The differing contrast and appearance of the surface layer relative to the bulk material may be due to Kapton impact since melting was not expected to occur at the surface of the Kr and Mo shot samples. EDS spectra for the bright surface layers again yielded high Fe and Ni signals. However, the Fe and Ni-rich surface layers were only observed in a few regions for the samples from the Kr/Mo shots; the sample from the Xe shot possessed Fe/Ni-rich regions throughout the entire sample surface.

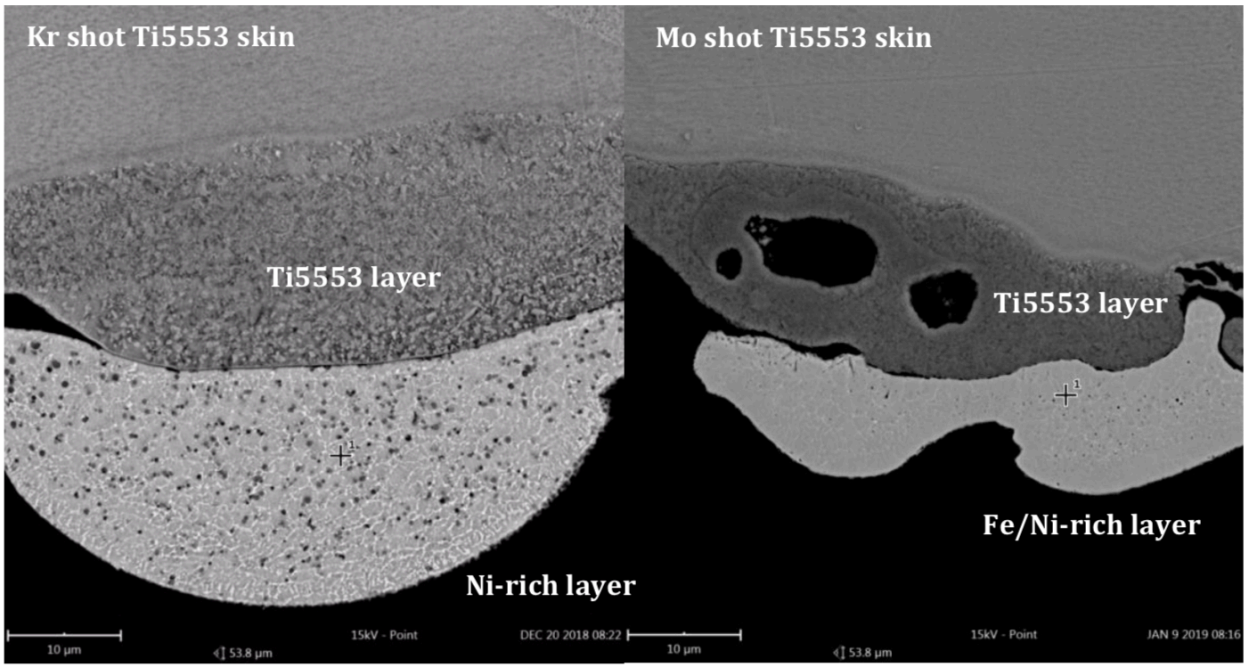

Figure 22: SEM images of Ti5553 skins from the Kr (left) and Mo (right) shots at the irradiated surface. Dark surface layers possessed similar EDS spectra to the reference Ti5553 spectrum. Bright surface layers showed strong Fe and Ni signals.

CONCLUSIONS

We have engineered snout and sample holder and filter, we have fielded experiments, we have measured data…

All Ti5553 skins and single skin lattice structures exhibited deformation as a result of each shot. Deformation of the single skin lattices was evidenced by numerous broken or deformed struts throughout the structures near the sample boundaries.
The Lattice material for the double skin structures appears unaffected by the Xe/Kr shots, while the sample from the Mo shot (18 keV peak energy) experienced deformation of the struts near the sample boundaries. Since deformation of the lattice structures was concentrated within regions beneath the area enclosed by the sample holder, the constraint imposed by the sample holder assembly may be responsible for the localized failure of struts near the sample boundaries. For future studies, it is recommended to consider whether the experimental design will result in localized failure within lattice structures. All samples exhibited surface layers at the irradiated faces. However, given the small depth of the surface layer (approximately <50 µm), these significant microstructural changes caused by the experiment are contained within the Ti5553 skins.
Stress-induced α" may be present within the deformed samples based on the acicular features present within the Ti5553 skins from the Xe and Mo shots. The formation of stress-induced α" would not be considered abnormal since it is reported as a deformation mechanism for Ti5553 with a primarily β microstructure [18]. The precipitation/growth of phases such as ω and α that are known to cause large increases in yield strength were not suggested by microhardness

measurements, suggesting no significant change to bulk material yield strength occurred as a result of the shots.

Fe/Ni contamination of the irradiated surface was observed for samples from each shot. One likely source of the contamination is ablation of the stainless steel sample holder. Contamination of sample surfaces from the Kr and Mo shots also occurred due to high velocity impact of the Kapton filter into the samples (≈1.7 ktap impulse expected due to Kapton for the Kr shot). As a result, the influence of x-ray irradiation on material microstructure and properties at the irradiated surface cannot be reliably deconvoluted from the effects of surface contamination. For future studies, protecting the sample surfaces from contamination after irradiation is desired for reliable evaluation of surface layers and near-surface material properties.

References

1. E. I. Moses, R. E. Bonanno, C. A. Haynam, R. L. Kauffman, B. J. MacGowan, and R. W. Patterson, Jr., Eur. Phys. J. D 44, 215 (2007).
2. C. A. Haynam, P. J. Wegner, J. M. Auerbach, M. W. Bowers, S. N. Dixit, G. V. Erbert, G. M. Heestand, M. A. Henesian, M. R. Hermann, K. S. Jancaitis, K. R. Manes, C. D. Marshall, N. C. Mehta, J. Menapace, E. Moses, J. R. Murray, M. C. Nostrand, C. D. Orth, R. Patterson, R. A. Sacks, M. J. Shaw, M. Spaeth, S. B. Sutton, W. H. Williams, C. C. Widmayer, R. K. White, S. T. Yang, and B. M. Van Wonterghem, Appl. Opt. 46, 3276 (2007).
3. K. B. Fournier, J. Celeste, V. Rekow, D. R. Bopp, M. J. May, J. H. Fisher, R. Horton, C. D. Newlander, P. Jenkins, and K. Trautz, "A test cassette for x-ray-exposure experiments at the National Ignition Facility," Rev. Sci. Instrum., 81 (2010).
4. K. B. Fournier, C. G. Brown, Jr., M. F. Yeoman, J. H. Fisher, S. W. Seiler, D. Hinshelwood, S. Compton, F. R. Holdener, G. E. Kemp, C. D. Newlander, R. P. Gilliam, N. Froula, M. Lilly, J. F. Davis, MAJ. A. Lerch, and B. E. Blue, "X-ray transport and radiation response assessment (XTRRA) experiments at the National Ignition Facility," Rev. Sci. Instrum., 87 (2016).
5. M. J. May, J. D. Colvin, G. E. Kemp, M. A. Barrios, K. Widmann, R. Benjamin, D. Thorn, P. Poole, and B. Blue, "Development of high intensity X-ray sources at the National Ignition Facility," Physics of Plasmas 25, 056302 (2018).
6. K. B. Fournier, M. J. May, J. D. Colvin, J. O. Kane, M. Schneider, E. Dewald, C. A. Thomas, S. Compton, R. E. Marrs, J. Moody, E. Bond, P. Michel, J. H. Fisher, C. D. Newlander, and J. F. Davis, "Multi-keV x-ray source development experiments on the National Ignition Facility," PHYSICS OF PLASMAS 17, 082701 (2010)
7. M. J. May, K. B. Fournier, J. D. Colvin, M. A. Barrios, E. L. Dewald, M. Hohenberger, J. Moody, J. R. Patterson, M. Schneider, K. Widmann, and S. P. Regan, "Bright x-ray stainless steel K-shell source development at the National Ignition Facility," Physics of Plasmas 22, 063305 (2015).
8. K. B. Fournier, M. J. May, J. D. Colvin, M. A. Barrios, J. R. Patterson, and S. P. Regan, "Demonstration of a 13-keV Kr K -shell x-ray source at the National Ignition Facility," PHYSICAL REVIEW E 88, 033104 (2013).
9. M. May, "Development of High Fluence X-Ray Sources at the National Ignition Facility," LLNL-PRES-740081, (2017) used with permission.

10. K. Widmann, “Development of High-Flux Hard X-Ray Sources on the National Ignition Facility,” International Workshop on Radiative Properties of Hot Dense Matter 2016.
11. Fisher, J.H., et al., Advanced X-ray Transport and Radiation Response Assessment (XTRRA) Modeling, Simulation, and Test Final Report, Fifth Gait Technologies, 2015, HDTRA1-13-C-0084.
12. Fournier, K.B., et al. X-ray transport and radiation response assessment (XTRRA) experiments at the National Ignition Facility. in 21st Topical Conference on High-Temperature Plasma Diagnostics. 2016. Madison, WI.
13. DebRoy, T., et al., *Additive manufacturing of metallic components – Process, structure and properties.* Progress in Materials Science, 2018.
14. Schwab, H., et al., *Microstructure and mechanical properties of the near-beta titanium alloy Ti-5553 processed by selective laser melting.* Materials & Design, 2016.
15. Coakley, J., et al., *Precipitation Processes in the Beta-Titanium Alloy Ti-5Al- 5Mo-5V-3Cr*. Journal of Alloys and Compounds, 2015.
16. Shekhar, S., et al. *Effect of solution treatment and aging on microstructure and tensile properties of high strength β titanium alloy, Ti–5Al–5V–5Mo–3Cr.* Materials and Design, 2015.
17. Unpublished results, 2018. Courtesy of Holly Carlton and Stephen Knaus.
18. Barriobero-Vila, P., et al., *An in situ investigation of the deformation mechanisms in a B-quenched Ti-5Al-5V-5Mo-3Cr alloy.* Materials Science & Engineering A, 2018.
19. Cao, S., et al. *Role of martensite decomposition in tensile properties of selective laser melted Ti-6Al-4V.* Journal of Alloys and Compounds, 2018.
20. G. Lutjering and J.C. Williams, *“Titanium” Engineering Materials and Processes, second ed.* 2007, Berlin.